



**HAL**  
open science

# Deformation and Plasticity of Materials under Extreme Conditions

Sébastien Merkel

► **To cite this version:**

Sébastien Merkel. Deformation and Plasticity of Materials under Extreme Conditions. Fei, Yingwei; Walter, Michael J. Static and Dynamic High Pressure Mineral Physics, Cambridge University Press (CUP), pp.239-265, 2022. hal-03891121

**HAL Id: hal-03891121**

**<https://hal.univ-lille.fr/hal-03891121v1>**

Submitted on 9 Dec 2022

**HAL** is a multi-disciplinary open access archive for the deposit and dissemination of scientific research documents, whether they are published or not. The documents may come from teaching and research institutions in France or abroad, or from public or private research centers.

L'archive ouverte pluridisciplinaire **HAL**, est destinée au dépôt et à la diffusion de documents scientifiques de niveau recherche, publiés ou non, émanant des établissements d'enseignement et de recherche français ou étrangers, des laboratoires publics ou privés.

# Deformation and plasticity of materials under extreme conditions

Sébastien Merkel

Univ. Lille, CNRS, INRAE, ENSCL, UMR 8207 - UMET - Unité Matériaux et Transformations, F-59000 Lille, France

## Abstract

Understanding mechanical properties and their microscopic origins is fundamental for multiple fields in condensed matter research. They are controlled by defects, dislocations, diffusion, as well as microstructures, which are not trivial to study under extreme conditions. This chapter summarizes the last 25 years of advances in high pressure devices, x-ray measurements, and data interpretation capabilities for addressing the deformation and plasticity of materials under extreme conditions, from experiments in large volume presses or diamond anvil cells, texture and stress analysis in powder x-ray diffraction, multi-grain crystallography, to self consistent models of materials behavior. Examples of applications are then provided in the fields of geophysics and materials science along with perspectives for studies of plastic deformation under extreme conditions in the coming years.

## 1 Introduction

Mechanical properties are important for a range of applications, from the design of materials with advanced properties to the dynamics of planetary interiors. The plastic behavior of solid is controlled by defects, dislocations, diffusion, as well as microstructures, a generic term describing the arrangement of a material from the nm to the cm scale. Microstructures in minerals, for instance, are important for the dynamics of the deeper layers of the Earth (Karato et al. 2000). For such application, materials of interest include the high pressure phase of Fe,  $\epsilon$ -Fe (Wenk et al. 2000, Lincot et al. 2016), bridgmanite and ferropericlase (Miyagi and Wenk 2016, Marquardt and Miyagi 2015, Girard et al. 2016, Nzogang et al. 2018), or post-perovskite (Merkel et al. 2007, Miyagi et al. 2010, Dobson et al. 2013), most of which are not stable under ambient pressure and temperature and should be studied *in-situ*. Hydrostatic pressure also induces phase transformations in metals. Titanium and zirconium, for instance, are hexagonal-close-packed metals under ambient conditions. Under high pressure, they transform to another hexagonal structure, the  $\omega$  phase, which is not compact and for which mechanical properties are poorly constrained (Yu et al. 2015, Wenk et al. 2013, Kumar et al. 2020). In other cases, high pressure has been used as a fine-tuning parameter for optimizing strength and grain sizes (e.g. Zhou et al. 2020). As such, the study of mechanical properties *in-situ* under extreme conditions is of general interest.

The last 25 years have seen tremendous advances in high pressure instruments coupled with synchrotron radiation that allow studies of microstructures and mechanical properties under high pressure and high temperature (Raterron and Merkel 2009). The group at the Geophysical Laboratory and H.-K. Mao

37 provided key contributions to this field, through the design of new methods and ground-breaking  
38 publications (e.g. Hemley et al. 1997, Mao et al. 1998, Wenk et al. 2000, Merkel et al. 2002). Nowadays,  
39 millimeter size samples are deformed in *large volume presses* (LVP) up to Earth's uppermost lower  
40 mantle pressures. High pressures and lower dimension samples are deformed and studied in *diamond*  
41 *anvil cells* (DAC). In all cases, samples are submitted to a macroscopic deformation to induce plasticity  
42 and deformation microstructures. Their properties are then studied *in-situ* using X-ray diffraction and  
43 imaging. X-ray radiography allows the measurement of macroscopic properties, such sample size and the  
44 applied macroscopic deformation. X-ray diffraction on polycrystals allows for extracting average sample  
45 properties by the study of lattice preferred orientations (LPO) and the average stress state. Multigrain X-  
46 ray diffraction (sometimes labeled as 3D-XRD) addresses single-grains inside a polycrystalline matrix  
47 and, in some cases, allows for measuring densities of defects such as dislocations. As such, the properties  
48 of deforming materials can be studied *in-situ*, in their stability field or conditions of application.

49 In this chapter, I will present the experimental techniques for the high pressure study of materials  
50 plasticity. I will start with a description of the experimental devices, then present the characterization  
51 techniques using in-situ X-rays, modeling using self-consistent calculations, sample results for Earth's  
52 and other materials, and perspectives for the years to come.

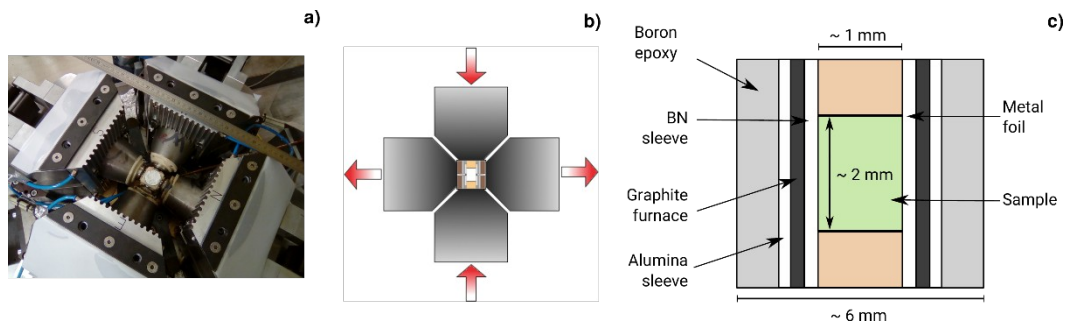
## 53 **2 Experimental techniques**

### 54 **2.1 Plasticity in the large volume press**

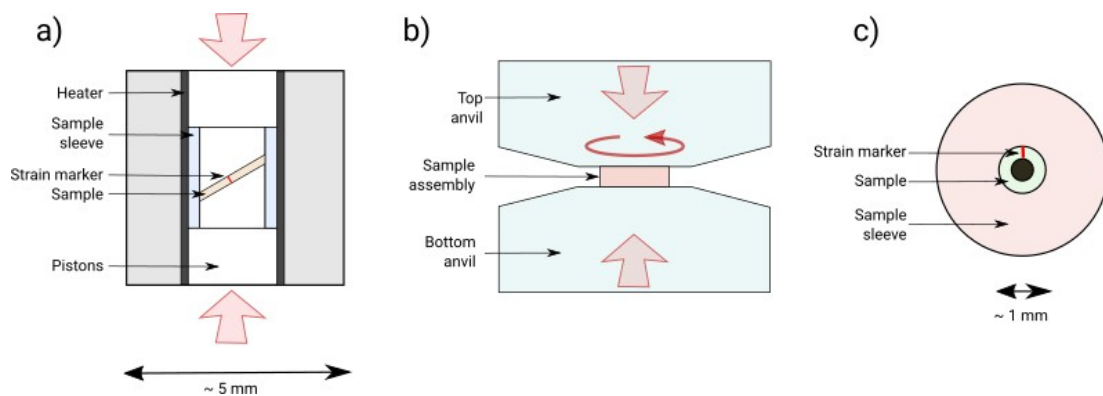
55 The Deformation-DIA (D-DIA), Rotational Drickamer (RDA), and deformation T-Cup (D-Tcup) are the  
56 main LVP for deformation experiments coupled with *in-situ* characterization under high pressure. All  
57 allow the controlled deformation of millimeter size samples. In addition, new apparatuses such as the  
58 RoToPEc (rotational tomographic Paris Edinburg cell) and high-pressure X-ray tomography microscope  
59 (HPXTM) are devices under development.

60 The D-DIA (Wang et al. 2003, Fig. 1) is a hydraulic press in which a cubic assembly is deformed under  
61 the action of 6 anvils. Heating sleeves allow temperatures up to  $\approx 2000$  K. Hydrostatic compression is  
62 obtained by advancing all 6 anvils (4 horizontal and 2 vertical) at the same velocity. Axial compression  
63 deformation at constant pressure is obtained by advancing the upper anvils while retracting the horizontal  
64 anvils. Lateral compression is obtained by retracting the vertical anvils and advancing the horizontal  
65 anvils. The D-DIA allows experiments at strain rates ranging from  $10^{-7}$  to  $10^{-2} \text{ s}^{-1}$  and pressures and  
66 temperatures up to 18 GPa and 1900 K (Kawazoe et al. 2013). It has also been adapted for deformation  
67 using a shear geometry up to 25 GPa and 1873 K (e.g. Fig 2a, Tsujino et al. 2016, Nishihara et al. 2018).  
68 Work is underway to develop new generations of D-DIA-like presses such as the D-DIA-30 allowing  
69 reaching higher pressures and working on larger samples (e.g. Wang and Shen, 2014). The D-TCup  
70 (Hunt et al. 2014, Hunt and Dobson 2017) is a similar setup with second stage anvils being developed to  
71 allow deformation experiments at pressures and temperatures exceeding those of the D-DIA. In all cases,

72 the imposed macroscopic strain of the cell assembly is axial and measured *in-situ* using X-ray  
 73 radiography (see below). Lateral macroscopic strain is reconstructed based on the axial macroscopic  
 74 strain and the sample's change of volume, deduced from x-ray diffraction.



75  
 76 Figure 1: (a) Main module of the D-DIA deformation press at the ID06 beamline of the ESRF  
 77 synchrotron. The main anvils, labeled as here E, W, N, and S, apply a load on secondary anvils to  
 78 generate deformation. The lower (hidden) and top (opened) anvils are not visible on the image. (b)  
 79 Principle of the D-DIA. Vertical and horizontal anvils can be moved independently. (c) Typical sample  
 80 assembly placed between the 6 anvils for deformation experiments. For simplicity, the thermocouples  
 81 measuring temperature are not shown.



82 Figure 2: Typical sample assemblies for shear deformation in the LVP. (a) Shear deformation in the D-  
 83 DIA (e.g. Tsujino et al. 2016). Axial strain (red arrows) is applied to the cell assembly, which translates to  
 84 shear strain on the sample. (b) Torsion in the RDA. Pressure is applied by advancing the top and bottom  
 85 anvils. The cell assembly is submitted to torsion by rotating one of the anvils. (c) Simplified top view of  
 86 the cell assembly in the RDA in Girard et al. 2016. The sample is a ring of 0.2 mm thickness, 0.45 mm  
 87 inner diameter and 1 mm outer diameter.

88 The rotational Drickamer (RDA, Fig. 2b) is an opposed anvil high pressure device that has been modified  
 89 to perform large strain deformation experiments in simple shear geometry (Yamazaki and Karato  
 90 2001). Samples can be sheared between two anvils under pressure by a rotation actuator, with strains  
 91 exceeding  $\gamma \approx 6$  at high pressure at strain rates similar to those of the D-DIA. Early sample designs used  
 92 disks of less than 0.8 mm thick and up to 4 mm outer diameter (e.g. Yamazaki and Karato 2001) while  
 93 recent experiments rely on rings of 0.2 mm thickness, 0.45 mm inner diameter and 1 mm outer diameter

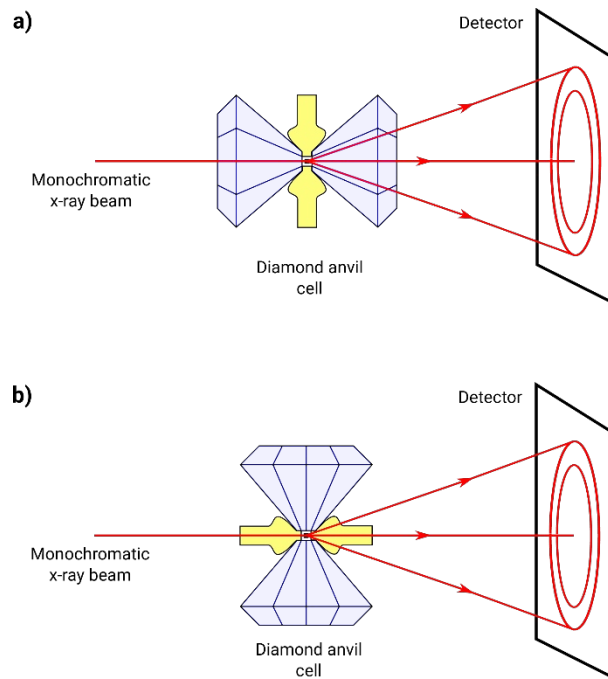
94 for a better control of sample strain (Fig 2c, Girard et al, 2016). The RDA was successfully used to obtain  
95 quantitative creep results on wadsleyite (Nishihara et al. 2008, Kawazoe et al. 2010, Farla et al. 2015),  
96 ringwoodite (Miyagi et al. 2014), and bridgmanite and magnesiowüstite aggregates (Girard et al. 2016) up  
97 to 27 GPa and 2150 K. In the RDA, the stress applied to the sample is evaluated using x-ray diffraction  
98 and is a combination of pure shear and axial compression (Xu et al. 2005).

99 New advances in the field also include the coupling deformation in simple shear using torsion devices  
100 such as the RoToPEc and HPXTM with tomographic measurements. Proofs of principles have been  
101 published (Philippe et al. 2016, Wang et al, 2011) and the devices are currently in use at synchrotron  
102 sources.

## 103 **2.2 Plasticity in diamond anvil cells**

104 Large volume presses allow controlled deformation at constant pressure and temperature but do not cover  
105 the entire range of conditions found in the Earth's interior. DAC, on the other hand, allow static  
106 experiments at pressures exceeding that at the center of the Earth (Dewaele et al. 2018) and combined  
107 pressures and temperatures of the Earth's core (Tateno et al. 2010). In addition to confining pressure,  
108 diamonds in the DAC impose an axial compressive stress. In most experiments, the compressive stress is  
109 reduced by using pressure media around the sample. In plasticity studies, this comes at a benefit that  
110 allows macroscopic deformation of the sample. Unlike deformation in LVP, however, pressure and  
111 deformation can not be decoupled. Deformation experiments in the DAC are not performed at constant  
112 pressure nor at controlled stress or strain rates. The total plastic strain in DAC experiments, estimated  
113 from the magnitude of texture evolution, is on the order of 10 to 30%. It is applied over a duration of 5  
114 minutes to a few hours, translating to a strain rate estimate ranging from  $10^{-5}$  to  $10^{-3} \text{ s}^{-1}$ .

115 In most DAC experiments, the sample properties are studied through the diamond anvils which are  
116 transparent over a broad range of wavelength, including X-rays (Fig. 3a). For plasticity studies, it can be  
117 useful to have the incoming x-ray beam perpendicular to the loading axis (Fig. 3b). In the early radial  
118 diffraction experiments, the sample itself served as a gasket material (Kinsland and Bassett 1977). The  
119 sample stress state however, was complex with large pressure gradients across the sample. The technique  
120 was then improved by the group at the Geophysical Laboratory with the use of beryllium gaskets  
121 (Hemley et al. 1997) for a better controlled sample pressure and stress state, and further improved with  
122 the use of amorphous boron / epoxy composite gaskets (Merkel and Yagi 2005). Early radial x-ray  
123 diffraction experiments were performed at ambient temperature (Hemley et al. 1997, Mao et al. 1998,  
124 Wenk et al. 2000, Merkel et al. 2002).



125  
 126 Figure 3: Geometries for x-ray diffraction DAC experiments. The axial geometry (a) is most common,  
 127 with the incident x-ray beam aligned with the compression direction. The radial geometry (b) is  
 128 commonly used in deformation experiments. The incoming and diffracted x-ray beams are perpendicular  
 129 to compression, and pass through an x-ray transparent gaskets made of beryllium or composite materials.

130 High temperature deformation studies have been attempted by combining laser heating and diffraction in  
 131 the radial geometry, with limited success due to large temperature gradients in the sample (Miyagi et al.  
 132 2008). In order to obtain homogeneous conditions of stress, pressure, and temperature, efforts were hence  
 133 invested in developing dedicated DAC systems combined with resistive heating allowing for radial x-ray  
 134 diffraction (Liermann et al. 2009, Immoor et al. 2020), sometimes also complemented with additional  
 135 laser-heating (Miyagi et al. 2013). Under ambient temperature, radial diffraction experiments reached  
 136 pressures of nearly 300 GPa (Hemley et al. 1997). Combined conditions of 62 GPa at 1400 K were  
 137 obtained in the resistive heating setup (Immoor et al. 2018) and 69 GPa at 2273 K for setups combining  
 138 laser and resistive heating (Miyagi et al, 2013).

139 In addition, deformation experiments can be performed using a rotational diamond anvil cell (rDAC). In  
 140 the rDAC, one of the diamond anvils is allowed to rotate which produces a torsional deformation like in  
 141 the RDA (Blank et al. 1984). The rDAC has the potential to achieve large-strain under ultra-high pressure  
 142 conditions while attaining a steady-state deformation (Levitas 2004, Nomura et al. 2017). To this day,  
 143 however, the use of the rDAC for true deformation experiments has been limited due to the complex  
 144 stress and strain field in rDAC experiments (Ma et al. 2006, Zarechnyy et al. 2012). The reliability of  
 145 rDAC experiments is being improved, with new anvil designs for slip-free experiments which could  
 146 considerably improve the usability of the technique (Azuma et al. 2017).

## 147 **2.3 Computational plasticity**

148 Experimental techniques can be limited. In particular, when addressing the plastic properties of minerals  
149 in planetary interiors, experiments are performed at strain rates that are orders of magnitude above those  
150 of nature. As such, numerical approaches can become useful to understand, model, and extrapolate  
151 materials behavior.

152 Plastic deformation is the results of the complex, collective behavior of a large collection of defects  
153 within a material microstructure. Until recently, this task was not within the reach of numerical techniques  
154 but recent developments open the door to such studies (e.g. Cordier et al. 2012, Boioli et al. 2017, Reali  
155 et al. 2019). Such methods go beyond the scope of the current chapter but a detailed description can be  
156 found in Cordier and Goryaeva (2018).

## 157 **3 In situ characterization techniques**

### 158 **3.1 Deformation**

159 In LVPs, the sample's macroscopic deformation is measured using X-ray radiography. Strongly x-ray  
160 absorbing samples are visible directly while, for less-absorbing samples, one places foils of gold,  
161 platinum, or molybdenum in the sample assembly (e.g. Fig. 1c). Based on the displacement, shortening,  
162 or tilting of the metal makers, one can then reconstruct the macroscopic deformation applied to the  
163 sample (e.g. Raterron and Merkel 2009, Farla et al. 2015). Strain vs. time plots are then used to evaluate  
164 the sample strain rate.

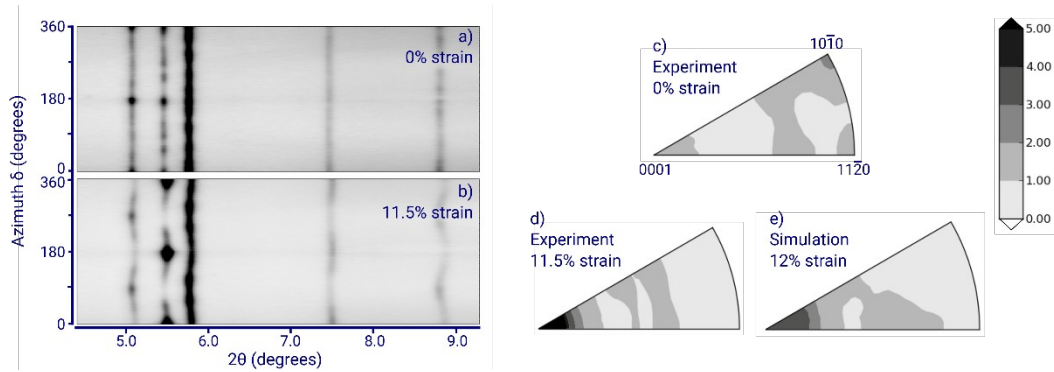
165 In DACs, deformation is rarely controlled and occurs during pressure increases. Moreover, the sample  
166 thickness is on the order of 20  $\mu\text{m}$ . Decent sample images can be obtained using changes in X-ray  
167 transmission contrasts (Merkel and Yagi 2005) but deformation are not very well resolved and, hence,  
168 these are rarely used. This could be improved using phase contrast imaging (e.g. Schropp et al. 2015)  
169 which allows for a much better resolved imaging of interfaces, and particularly so at upgraded  
170 synchrotron sources such as ESRF-EBS with an improved performance by a factor of 100 in beam  
171 coherence. To my knowledge, this has not been attempted yet.

### 172 **3.2 Polycrystal properties**

173 Powder x-ray diffraction is a standard technique for assessing average macroscopic sample properties,  
174 and can be applied to both DAC and LVP experiments. The diameter of the incident x-ray beam and  
175 sample microstructures, however, should be adjusted so that a statistically relevant number of grains  
176 contribute to the diffraction signal. Otherwise, statistical assumptions with the powder x-ray diffraction  
177 processing methods will fail and may lead to inconsistent results.

### 178 3.2.1 Lattice preferred orientations

179 Often, crystallites in a polycrystal are not randomly distributed in orientation and materials develop *lattice*  
180 *preferred orientations* (LPO). LPO can arise from processes such as nucleation, phase transformation, or  
181 plastic deformation. LPO have a strong influence on mechanical properties as physical properties become  
182 anisotropic (Kocks et al. 1998). They also affect the propagation of seismic waves and are hence of great  
183 interest in geosciences (Mainprice et al. 2000).



184

185 Figure 4: Diffraction images for  $\epsilon$ -Fe at 17 GPa and 400 K (Merkel et al. 2012) measured at the start of the deformation (a) and after 11.5% axial strain in a D-DIA (b). Variations of peak intensities and  
186 positions with azimuth are indicative of the sample LPO and stress, respectively. Measured inverse pole  
187 figure of the compression direction at the start of deformation (c) and after 11.5% axial strain (d). (e)  
188 Results of a self-consistent model after 12% axial strain reproducing the measured sample strain and  
189 textures and constraining the strength of basal, prismatic and pyramidal slip as well as tensile twinning in  
190  $\epsilon$ -Fe at those conditions.  
191

192 In high pressure deformation experiment, LPO measurements are often used to constrain plastic  
193 deformation mechanisms (Wenk et al. 2006). In fact, plastic deformation mechanisms and, in particular,  
194 dislocation glide will give rise to specific LPO in a polycrystals. LPO measurements, combined with  
195 texture modeling (see below) allow the identification of the active plastic deformation mode in a material.

196 Sample LPO appear as variation of diffraction intensities with orientation (Fig. 4) and can be extracted  
197 from the diffraction images using either Multifit (Merkel and Hilairet 2015) and BEARTEX (Wenk et al.  
198 1998) or MAUD (Lutterotti et al. 1999, Wenk et al. 2014).

### 199 3.2.2 Stress and strains

200 Stress-strain and stress-pressure curves are a critical element to characterize the mechanical properties of  
201 materials. In-situ determination of stress, however, is not trivial in high pressure experiments. Unlike  
202 classical, low pressure, deformation experiments, the applied stress is not measured directly. Early  
203 publications estimated stress based on pressure gradients across a relatively large sample (e.g. Meade and  
204 Jeanloz, 1988), with the limitation that pressure and stress is heterogeneous in such sample, leading to  
205 discrepancies with other measurements (Reynard et al. 2019). Internal quartz calibrants can be used for  
206 in-situ piezometry in the DAC. Raman vibrational mode frequencies shift with pressure and deviatoric



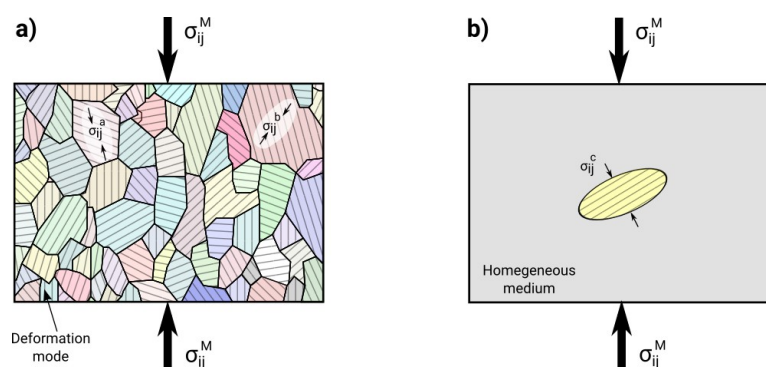
207 stresses induce TO-LO splitting of the lowest frequency E mode of quartz. All have been calibrated  
208 recently (Reynard et al. 2019). Most high pressure deformation experiments, however, rely on in-situ x-  
209 ray diffraction for stress evaluation.

210 Residual stress analysis using x-ray diffraction is a common technique in materials science (Noyan and  
211 Cohen 1987) and was adapted to high pressure research in the mid-1990's (e.g. Hemley et al. 1997, Singh  
212 et al. 1998). Hydrostatic pressure changes the unit cell parameters of a material, and hence the average d-  
213 spacings of all powder x-ray diffraction lines. Deviatoric stresses add an additional component with  
214 changes of the measured d-spacings with orientation (Fig. 4a). Theories relating deviatoric stress and the  
215 measured strains using x-ray diffraction are available in the literature, both for axial (Singh et al. 1998)  
216 and shear (Nishihara et al. 2008) deformation experiments. All rely on elasticity theory and assume  
217 continuity of stress or strain within the deforming aggregate.

218 The elastic assumption for stress inversion, however, fails when plastic deformation is at play (Li et al.  
219 2004, Merkel et al. 2006). In fact, as materials deform, stresses will relax in grains in soft orientations (i.e.  
220 for which plastic deformation can be easily activated) while other grains, whose orientations do not favor  
221 plastic deformation, will remain highly stressed. For each orientation, the measured d-spacing in powder  
222 x-ray diffraction is the average d-spacing of all grains contributing to the diffraction, either soft or hard.  
223 This heterogeneity of stress within grains contributing to the same diffraction peak is not well captured by  
224 elasticity-based models. The average stress state and intergranular stress heterogeneities in a deforming  
225 material, however, can be modeled using self-consistent techniques (see below, Fig. 7).

226 Another approach to circumvent the issue of stress evaluation using X-ray diffraction is to use an internal  
227 standard.  $\text{Al}_2\text{O}_3$ , for instance, is well-known and was calibrated using self-consistent techniques (Raterron  
228 et al 2013). Pyrope is another option as experiments have shown that it is plastically isotropic with less  
229 than 10 % variation for stresses deduced between different diffraction lines (e.g. Girard et al 2020).

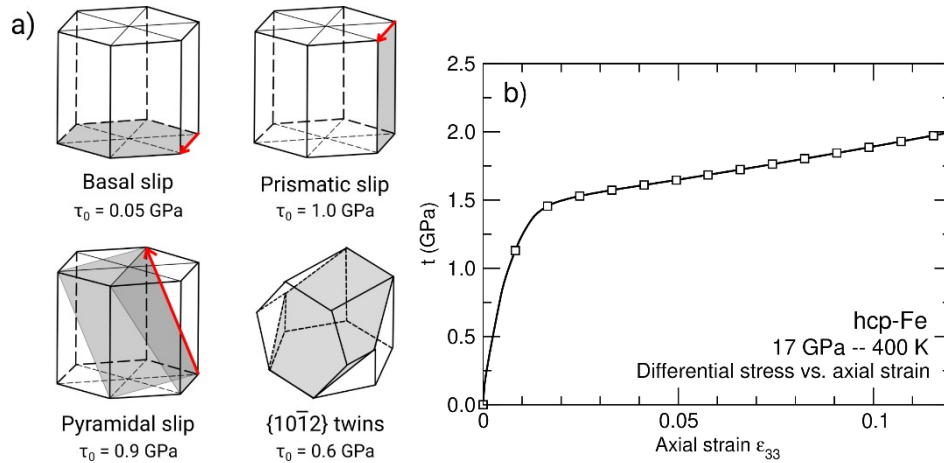
### 230 3.2.3 Interpretation using self-consistent models



231  
232 Figure 5: Polycrystalline simulation (after Amodeo et al. 2018). (a) In a polycrystal, stress and strain  
233 distributions are heterogeneous. The behavior of each grain depends on its local environment, elastic, and  
234 plastic properties. (b) In self-consistent models, each grain is treated as an elliptical inclusion inside a  
235 homogeneous medium.

236 Deformation experiment are best interpreted using self-consistent (SC) methods. SC calculations treat  
 237 each grain of the polycrystal as an inclusion in a homogeneous but anisotropic medium (Fig. 5). The  
 238 properties of the medium are determined by the average of all inclusions. At each deformation step, the  
 239 inclusion and medium interact and the macroscopic properties are updated iteratively until the average  
 240 strain and stress of all inclusions equals the macroscopic strain and stress.

241 The Elasto-Plastic Self-Consistent (EPSC) approximation of Turner and Tomé (1994), later extended by  
 242 Clausen et al. (2008) and Neil et al. (2010), accounts for elasticity of the material as well as stress  
 243 relaxation and grain rotation due to twinning and dislocation slip. Plasticity in EPSC calculations,  
 244 however, is not dependent on strain rates. Visco-Plastic Self-Consistent (VPSC) calculations account for  
 245 stress relaxation and grain rotation due to twinning and dislocation slip, accounting for a strain-rate  
 246 dependent plasticity, but do not account for elasticity (Lebensohn and Tomé 1994). Finally, the Elasto-  
 247 Visco-Plastic Self-Consistent (EVPSC) formulation, such as in Wang et al. (2010), accounts for elastic  
 248 stresses, grain rotation, and relaxation due to plasticity, as well as strain rate dependence of the plastic  
 249 behavior.



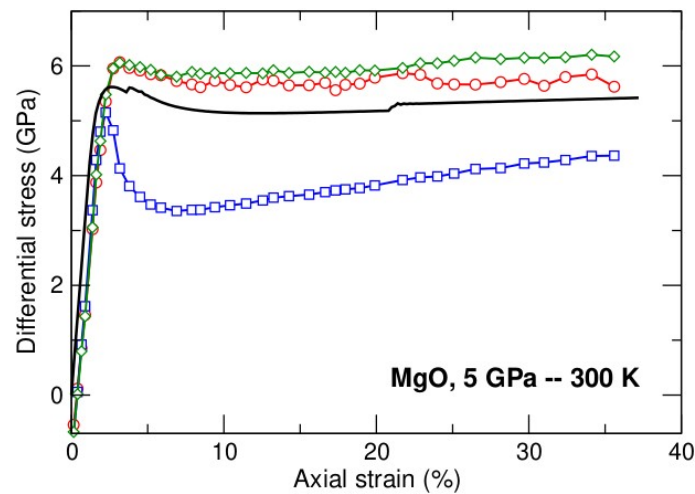
250  
 251 Figure 6: Plasticity of  $\epsilon$ -Fe at 17 GPa and 400 K (after Merkel et al. 2012). (a) Dominant deformation  
 252 mechanisms deduced from the data in Fig. 4.  $\tau_0$  is the initial CRSS, before hardening later in the  
 253 deformation. (b) Differential stress vs. axial strain.

254 All SC calculations can be used to model the evolution of polycrystalline textures. Comparing the  
 255 experimentally measured LPO and the results of SC calculations allows for the identification of dominant  
 256 plastic deformation mechanisms and, in particular, dislocation slip or twinning. VPSC calculations,  
 257 however, will not model macroscopic or intergranular stress, nor lattice strains measured in experiments.  
 258 EPSC or EVPSC will allow interpreting both the experimental texture and lattice strains (Merkel et al.  
 259 2009, Lin et al. 2017, Li et al. 2004).

260 For  $\epsilon$ -Fe at 17 GPa and 400 K, for instance, a comparison between experimental data and the results of  
 261 EPSC models indicates that plastic deformation is dominated by the activity of basal slip and  $\{10\bar{1}2\}$   
 262 tensile twinning (Fig. 6). The critical resolved shear stress (CRSS) of basal slip is low (0.05 GPa) but, due

263 to intergranular interactions and effects of grain orientations, the overall macroscopic stress reaches  
264  $t=2.0$  GPa after 12% axial compression.

265 Fig. 7 highlights one of the advantages on self-consistent models for analyzing the results of high  
266 pressure deformation experiments. Stresses deduced from elastic models are inconsistent due to stress  
267 heterogeneities between grains in soft orientations, for which stresses are relaxed through plastic  
268 deformation, and grains in hard orientations, which experience a higher stress. The results in an apparent  
269 stresses that can vary by up to 50% or more depending on the choice of measurement which will, later,  
270 translate into inconsistent flow laws. One should keep in mind, however, that x-ray diffraction is sensitive  
271 to strains at the local scale, for grains contributing to diffraction, and not stress. Self-consistent  
272 calculations (EVPSC in Fig. 7) allows determining the true stress value, consistent with all strain  
273 measurements using x-ray diffraction.

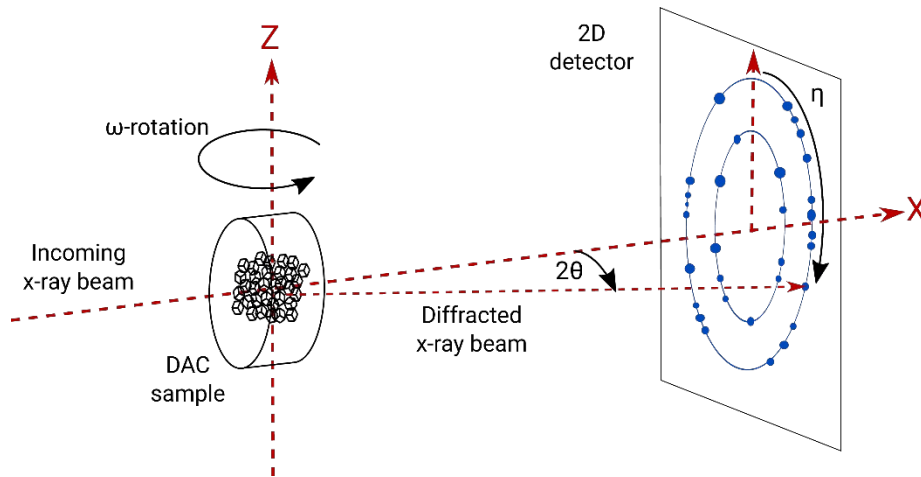


274 Figure 7: Stress in polycrystalline MgO plastically deformed at 5 GPa and 300 K in the D-DIA (Lin et al.  
275 2017). The plot displays apparent stresses deduced from an elastic model and x-ray diffraction  
276 measurements on the 111, 200, and 220 diffraction lines. Solid back line is the result of EVPSC  
277 calculations. Plastic deformation results in different stress values in the elastic model, which is  
278 inconsistent: average stress in the polycrystal should be unique. This can be solved by modeling the  
279 experiment using self-consistent calculations.

### 280 3.3 Plasticity at the grain scale

281 Recently, experimental studies of microstructures and plastic deformation reached a new milestone with  
282 techniques allowing the characterization of individual grains or subgrains within a polycrystalline  
283 material (Ludwig et al. 2009). Multigrain x-ray diffraction allows for a rapid, in-situ, and non-destructive  
284 study of microstructural elements. These elements can also be followed in situ as a function of time or  
285 external parameters such as stress, pressure, or temperature. Moreover, samples in high pressure  
286 experiments and, in particular, those of DAC are often small and do not contain enough grains for a

287 statistically relevant powder diffraction analysis. They are, on the other hand, perfectly suited for  
288 multigrain x-ray diffraction.



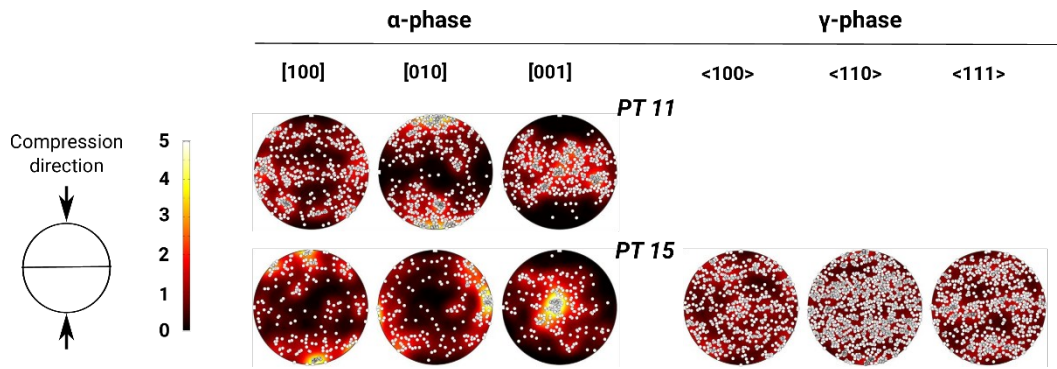
289  
290 Figure 8: Setup for multigrain crystallography at high pressure. The sample is confined in a DAC in axial  
291 geometry with an  $\omega$  rotation parallel to the Z direction. Diffraction patterns are collected on a flat panel  
292 detector orthogonal to the incoming X-ray beam over  $\Delta\omega$  ranges of  $\approx 50^\circ$  in steps of  $\delta\omega \approx 0.5^\circ$ . Individual  
293 grains inside the polycrystalline sample give rise to diffraction spots at specific  $2\theta$ ,  $\omega$ , and  $\eta$  angles.

### 294 3.3.1 Multigrain crystallography

295 Multigrain x-ray diffraction allows for the extraction of the orientation and crystal structure of hundreds  
296 of elements inside a polycrystalline material (Poulsen 2004). Extensions of the technique further allow the  
297 determination of the position and stress state for each of those elements (Oddershede et al. 2010).

298 The method has been applied to DAC experiments (Nisar et al. 2012, Rosa et al. 2016, Zhang et al. 2014,  
299 Langrand et al. 2017) including pioneering works involving H.-K. Mao (Ice et al. 2005). The method is  
300 not restricted to DAC experiments and could also be applied to LVP experiment but this remains to be  
301 reported. Multigrain x-ray diffraction consists in a search for diffraction spots while exploring reciprocal  
302 space (Fig. 8). A first analysis generates a database of experimental diffraction spots, along with their  $2\theta$ ,  
303  $\omega$ , and  $\eta$  angles and intensities. Algorithms such as GrainSpotter (Schmidt 2014) then use the  
304 experimental diffraction spots database and scan the grain orientation space to reconstruct the number and  
305 orientations of the individual diffracting sample grains.

306 In the work of Rosa et al. (2016), for instance, we used multigrain x-ray diffraction in order to study the  
307 effect of olivine-wadsleyite-ringwoodite chain of phase transformations on microstructures up to 22 GPa  
308 and 940 K. We follow the number of grains for each phase, their orientations, a distribution of grain sizes,  
309 at each step of the phase transformation (Fig. 9). Such measurement allow the study of phase  
310 transformation mechanisms and associated microstructures, with important applications for constraining  
311 deep-Earth processes. They can, as well, be extended to follow microstructures induced by plastic  
312 deformation.

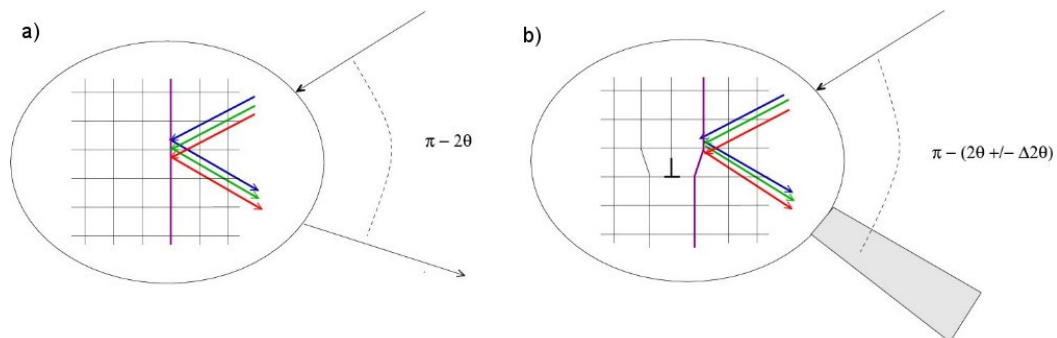


313

314 Figure 9: Sample results from multigrain crystallography in the DAC (Rosa et al. 2016). Pole figures  
 315 presenting the orientations of individual olivine and ringwoodite grains during a phase transformation at  
 316  $\approx 18$  GPa and 880 K. White circles are individual grain orientations. Background color scale is  
 317 recalculated based on an orientation distribution function fitted to sample. Scale in m.r.d. (multiples of a  
 318 random distribution).

### 319 3.3.2 Defects

320 X-ray line profile analysis (XLPA) is an effective technique for the study of grain level microstructures  
 321 using x-ray diffraction (Kerber et al. 2011). The shape of Bragg diffraction peaks can be quantitatively  
 322 evaluated not only in terms of the crystallite size and its distribution, but also in terms of the density, type  
 323 and arrangement of dislocations, twins and stacking faults (e.g. Fig. 10).



324

325 Figure 10: Principles of defect analysis using x-ray diffraction. Unlike a perfect crystal (a), defects such  
 326 as dislocations induce a local distortion of the crystal structure (b). The presence of defects induces a  
 327 broadening of the x-ray diffraction peak which, unlike that of grain sizes for instance, is anisotropic and  
 328 depends on the hkl indices of the reflection and the type of dislocation.

329 The advantages of the XPLA method are that *i*) the resolution increases with a decreasing grain size and  
 330 increasing defect density, and *ii*) it relies on x-ray diffraction and can hence be applied to high pressure  
 331 experiments. The effect of dislocations on peak broadening, for instance, can be measured when their  
 332 density increases above  $10^{12} \text{ m}^{-2}$ . On the other hand, it requires a high angular resolution (below  $0.01^\circ$ )  
 333 and relative accuracy of  $10^{-4}$  on diffraction intensities at the edges of diffraction peaks. Also note that,  
 334 unlike techniques such as high resolution back-scattered electron diffraction (HR-EBSD), XLPA is

335 sensitive to the total dislocation density, including both geometrically necessary and statistically stored  
336 dislocations (Ribárik et al, 2019) and can not distinguish between both.

337 Under high pressure, the XPLA technique, combined with multigrain crystallography was used for the  
338 study of dislocations in deep Earth materials. Experiments on  $\text{MgGeO}_3$  in the post-perovskite structure,  
339 for instance, allowed the identification of dominant dislocation types in this material at 90 GPa (Nisr et al.  
340 2012).

## 341 **4 Sample results**

### 342 **4.1 Deep Earth materials**

343 Iron is one of the most abundant metals, a widely used technological material, and the main constituent of  
344 the Earth's core. As such, the plastic properties of iron under pressure and temperature have received  
345 much attention during the past decades. Nothing was known on the plasticity of  $\epsilon$ -Fe in the mid-1990's  
346 and geophysical models of inner-core behavior often relied on simple assumptions such as the  
347 comparison of  $c/a$  ratios between  $\epsilon$ -Fe and other hcp metals (e.g. Jeanloz and Wenk 1988). Pioneering  
348 works were performed at the Geophysical Laboratory with radial x-ray diffraction on Fe up to 220 GPa  
349 (Mao et al. 1998) and paved the way to the determination of the plastic properties of  $\epsilon$ -Fe under high  
350 pressure (Wenk et al. 2000, Merkel et al. 2004, 2012, Gleason and Mao 2013, Nishihara et al. 2018).

351 Our current understanding is that basal slip and tensile twinning are the dominant plastic deformation  
352 mechanism of  $\epsilon$ -Fe at high pressure and room temperature (Wenk et al. 2000, Merkel et al. 2012). The  
353 strength of each deformation was characterized with D-DIA measurements at 13–17 GPa and 400–700 K  
354 (Merkel et al. 2012, Nishihara et al. 2018). These new interpretations also highlight the important  
355 contribution of tensile twinning to understand the evolution of stress and texture at those conditions.  
356 Measurements up to 200 GPa at ambient temperature combined with a numerical model also indicate that  
357 the bulk shear strength of Fe is  $\approx 1$  GPa at inner-core pressures and temperatures (Gleason and Mao 2013).  
358 This suggests that the inner core is rheologically weak and supports dislocation creep as the dominant  
359 creep mechanism influencing deformation. Deformation experiments on Fe, however, have only reached  
360 pressures of  $\approx 200$  GPa at ambient temperature and combined pressure and temperatures of  $\approx 17$  GPa and  
361  $\approx 700$  K. These remain far from those in the inner core (above 300 GPa and 5000 K). Future efforts will be  
362 hence invested in extending the pressure and temperature range of experiments analyzing the plastic  
363 behavior of Fe.

364 Ferropericlase,  $(\text{Mg,Fe})\text{O}$ , is another interesting material regarding high pressure plasticity studies.  $\text{MgO}$   
365 is a very well-known crystalline ceramic whose mechanical properties are thoroughly studied in materials  
366 science (Amodeo et al. 2018), both experimentally (e.g. Korte and Clegg 2011, Tromas et al. 2000) and  
367 using numerical plasticity techniques (e.g. Amodeo et al. 2012, Cordier et al. 2012).  $(\text{Mg,Fe})\text{O}$  is also the  
368 second dominant phase in the Earth's lower mantle. For the above reasons, numerous studies of the  
369 plastic properties of  $(\text{Mg,Fe})\text{O}$  under high pressure and temperature can be found in the literature (e.g.

370 Merkel et al. 2002, Cordier et al. 2012, Amodeo et al. 2012, 2016, Yamazaki and Karato 2002, Tommaseo  
371 et al. 2006, Lin et al. 2009, Long et al. 2006, Mei et al. 2008, Uchida et al. 2004, Lin et al. 2017,  
372 Marquardt and Miyagi 2015, Immoor et al. 2018, Kinsland and Bassett 1977, Lin et al. 2019, Girard et al.  
373 2012, Heidelbach et al. 2003, Stretton et al. 2001).

374 Under ambient temperature, pure MgO deforms through dislocation slip on  $\{110\}\langle 1\bar{1}0\rangle$  (Merkel et al.  
375 2002, Lin et al. 2017) with an increased activity of  $\{110\}\langle 100\rangle$  with increasing temperature (Paterson  
376 and Weaver 1970). Recent calculations also predict a transition between  $\{110\}\langle 1\bar{1}0\rangle$  and  $\{110\}\langle 100\rangle$   
377 slip with increasing pressure (Amodeo et al. 2012) and that, moreover, in the Earth's mantle, extremely  
378 low strain rates counteract the influence of pressure with MgO deforming in the athermal regime where  
379 dislocation motion is purely controlled by dislocation interactions rather than lattice friction (Cordier  
380 et al. 2012). Deformation experiments on single crystal do show a trend consistent with such change of  
381 slip system with pressure (Girard et al. 2012) and deformation experiments on ferropiclasite show  
382 evidence of both  $\{110\}\langle 1\bar{1}0\rangle$  and  $\{110\}\langle 100\rangle$  slip at  $\approx 1400$  K in a range of 30–60 GPa (Immoor et al.  
383 2018). Recent ambient temperature measurements and modeling on pure MgO up to 50 GPa, however,  
384 predict an increasing activity of  $\{110\}\langle 1\bar{1}0\rangle$  slip with pressure (Lin et al. 2019). As such, the effect of  
385 pressure (and strain rate) on the plasticity of pure MgO remains an active field of research.

386 The addition of Fe in (Mg,Fe)O does not seem to drastically affect the type of dominant slip systems in  
387 (Mg,Fe)O (Tommaseo et al. 2006, Long et al. 2006, Yamazaki and Karato 2002, Stretton et al. 2001,  
388 Immoor et al. 2018). Between 40 and 80 GPa however, Fe in (Mg,Fe)O undergoes electronic spin-pairing  
389 transition from a high-spin to a low-spin state (Badro et al. 2003) with potential effects of on sample  
390 stress (Lin et al. 2009). Measurements up to 100 GPa at ambient temperature also seem to indicate that  
391 the strength of (Mg,Fe)O increases by a factor of three at pressures from 20 to 65 GPa (Marquardt and  
392 Miyagi 2015) with important consequences regarding the stagnation of slabs sinking through the shallow  
393 lower mantle. These conclusions remain to be confirmed at mantle temperatures and strain rates.

## 394 4.2 Materials science

395 Simple metals were quickly recognized as a field of study regarding high pressure mechanical properties  
396 (e.g. Re, Mo and Au, Duffy et al. 1999b, 1999a). These first publications were followed by studies on Pt  
397 (Kavner and Duffy 2003), Os (Chen et al. 2010a, Weinberger et al. 2008), Gd (Xiong et al. 2014), W (He  
398 and Duffy 2006, Xiong et al. 2018), Co (Merkel et al. 2009), or Al (Singh et al. 2007), slowly constituting  
399 a database of strength and deformation mechanisms in simple metals as a function of pressure. It turns out  
400 that the yield strength of Os is significant larger than that of other stiff pure metals ( $\approx 12$  GPa at 60 GPa),  
401 followed by Re and W. Other metals, such as Ti or Zr, undergo phase transitions at relatively low  
402 pressure. This motivated studies of texture and strength, both during the phase transformation and for the  
403 higher pressure phase. Wenk et al. (2013), for instance, studied the  $\alpha \leftrightarrow \omega$  transition in Zr and found *i*) a  
404 martensitic mechanisms with  $(0001)_{\alpha} \parallel (11\bar{2}0)_{\beta}$  and *ii*) remarkable orientation memory during the

405 reverse transformation. This was then followed by further studies on the  $\alpha \leftrightarrow \omega$  transition in Zr and the  
406 mechanical properties of both phases (Yu et al. 2015, Kumar et al. 2020), with the aim to design Zr  
407 microstructure and strengthen its mechanical properties for high-pressure applications.

408 The Hall-Petch relationship predicts that the strength of materials should increase with smaller grain  
409 sizes. It is verified down to grain sizes of about 30 nm for which an inverse Hall-Petch effect is often  
410 observed, with a decrease of strength with decreasing grain size. This inverse Hall-Petch effect is  
411 attributed to a transition from dislocation-based plasticity to grain boundary sliding, rotation, or diffusion  
412 but this remains controversial (Naik and Walley 2020). This motivated studies on the effect of grain sizes  
413 on the plastic behavior of nanocrystalline materials under pressure (e.g. Singh et al. 2008). The  
414 application of hydrostatic pressure is found to have a strong effect on the transition from the Hall-Petch to  
415 inverse Hall-Petch effect. In fact, evidences for dislocation activity were observed in 3 nm Ni compressed  
416 to 18.5 GPa (Chen et al. 2012). Moreover, recent work on pure Ni report a continuous strengthening in  
417 samples with grain sizes from 200 nm down to 3 nm, with the strengthening enhanced (rather than  
418 reduced) at grain sizes smaller than 20 nanometres (Zhou et al. 2020). These recent works await  
419 confirmation in other materials and a better understanding of the combined effect of pressure and grain  
420 sizes on dislocation-based plasticity. They do, however, illustrate how studies under high pressure can  
421 help solve fundamental issues in materials science.

422 Other applications in materials science include the design of new, strong materials either as pure phases  
423 (Xiong et al. 2013, Kiefer et al. 2005, Dong et al. 2009, He et al. 2004, Liermann et al. 2007, Chen et al.  
424 2010b) or with a controlled microstructure (Conil and Kavner 2006), as well as the peculiar effect of  
425 phase transitions on microstructures in oxides (Yue et al. 2016). All remain an active field of study.

## 426 **5 Perspectives**

### 427 **5.1 Multiphase aggregates**

428 The vast majority of rocks that constitute the Earth are not made of a single material but rather an  
429 assemblage of multiple minerals. The microstructure, i.e. the arrangement of each phase, the orientation  
430 and size of each grain, has an influence on the overall mechanical properties of the rock. As such, the  
431 mechanical properties of multiphase aggregate are of great interest for the geosciences. They are also  
432 fundamental to materials science application, for which the design of composite materials with a pre-  
433 defined microstructure and physical properties are of great interest. Despite their relevance however, the  
434 mechanical properties of polyphase aggregates under pressure remain poorly understood.

435 In the Earth's lower mantle, for instance, bridgmanite is substantially stronger than ferropericlase and  
436 experiments indicate that ferropericlase accommodates most of the strain (Wang et al. 2013, Miyagi and  
437 Wenk 2016, Girard et al. 2016). A simple approach indicates that, if the weaker ferropericlase is not  
438 interconnected, then rheology of the lower mantle will mostly depend on bridgmanite, but if  
439 ferropericlase is interconnected, then it will control deformation. The microstructural arrangement of



440 bridgmanite and ferropericlasite, however, is controlled by plastic deformation, which in turn, is controlled  
441 by the properties of both phases. It is therefore required to understand this complex interplay between  
442 microstructure, the properties of each phase, and the material's macroscopic response. Moreover, stress  
443 percolates through polycrystalline materials that have heterogeneous elastic and plastic properties. The  
444 pattern of stress percolation is related to the degree of heterogeneity in and statistical distribution of the  
445 elastic and plastic properties of the constituent grains in the aggregate (Burnley 2013). To this day, the  
446 understanding and modeling of the feedback between single phase plasticity, microstructures, and  
447 macroscopic behavior of multiphase materials remains a challenge that has seldomly been attempted in  
448 high pressure research (Kaercher et al. 2016, Kasemer et al. 2020).

449 In addition, pressure, temperature, and deformation can induce mineralogical reactions which will affect  
450 the mechanical properties of the aggregate. In olivine + serpentines aggregates, for instance, it has been  
451 shown that dehydration reactions of deforming samples containing only 5 vol% of antigorite suffices to  
452 trigger significant stress transfer and embrittlement (Ferrand et al. 2017). A strong weakening of cold  
453 subducting slab was also reported due to the olivine to ringwoodite phase transformation (Mohiuddin et  
454 al. 2020). The mechanical properties of aggregates undergoing phase transformations are relevant for  
455 mantle dynamics and the generation of deep earthquakes deep inside the Earth. Such approach could,  
456 also, find multiple application for the understanding of mechanical properties of materials undergoing  
457 phase transformations at other conditions of extreme pressure and temperature.

## 458 **5.2 Technical developments**

459 This chapter mostly focused on coupling in-situ deformation, x-ray diffraction, and radiography. In the  
460 coming years, high pressure deformation studies could greatly benefit from further technological  
461 developments. For the study of deep earthquakes for instance, the D-DIA deformation press has been  
462 coupled with devices recording the sample's acoustic emissions during deformation (Schubnel et al.  
463 2013). The acoustic emission signals can even be further processed to understand the nature of the focal  
464 mechanisms, their distribution in both space and time during deformation, and further waveform analysis  
465 could be possible (Wang et al. 2017). The combination of high pressure plastic deformation experiments  
466 with the tracking of the sample's acoustic emissions could be of great interest for high pressure plasticity  
467 studies. In fact, plastic mechanisms such as twinning or dislocation slip are known to trigger acoustic  
468 emissions in ambient pressure deformation experiments (Weiss et al. 2000, Vinogradov et al. 2016,  
469 Muránsky et al. 2010) and this field of study could open new doors to high pressure research.

470 Presently, strain measurements in DAC deformation experiments is limited to average measurements in  
471 polycrystals. Multigrain crystallography allows strain mapping at the grain level (Oddershede et al. 2010)  
472 and can be used, for instance, to evaluate strain localization in deformation experiments (Sedmák et al.  
473 2016). Strain mapping using multigrain crystallography has been tested in DAC experiments (Nisr et al.  
474 2014) but the method remains to be strengthened, tested, and applied to topics such as stress percolation  
475 in heterogeneous aggregates.

476 Advanced imaging techniques, often relying on the high coherence of synchrotron x-ray beams, such as  
477 Bragg coherent diffractive imaging, ptychography, or dark-field x-ray microscopy, allow for revealing  
478 strains and heterogeneities within a single grain (Yau et al. 2017, Hruszkewycz et al. 2016, Simons et al.  
479 2015), may be used under operando conditions, and some have been tested in DAC experiments (Yang  
480 et al. 2013). These proof-of-concept experiments show that three-dimensional strain distribution with a  
481 spatial resolution of 30 nm can be measured inside a 400 nm crystal within a DAC. At present, these  
482 techniques represent a steep technical challenge but, with the advent of new, powerful, and highly  
483 coherent sources at ERSF, PETRA, SPRING-8, and APS, may become more routine measurements in the  
484 future. Local strain mapping techniques allowing, for instance, the determination and mapping of  
485 dislocation types and densities (Wallis et al. 2017) could then be performed in situ under high pressure.

486 3D X-ray tomography also offers avenues for new experiments in LVP (e.g. Urakawa et al. 2010, Wang et  
487 al. 2011, Philippe et al. 2016, Yu et al. 2016) with the ability to resolve small heterogeneities under high  
488 pressure and temperature and various strain conditions. This allows in situ tracking of various  
489 components in complex materials, with implications on their mechanical properties, connectivity, or  
490 permeability. Wang et al (2011) and Todd et al (2016), for instance, studied the effect of deformation on  
491 microstructures of metal-silicate aggregates with implications for the mechanical properties of composite  
492 materials relevant to the Earth's mantle and the formation of planetary cores. One could also refer to  
493 ongoing work on serpentines-olivine aggregates, with implications for subduction zones (Mandolini et  
494 al. 2020) or the in-situ monitoring of the orientations and mobility of interfaces during phase transitions  
495 (e.g. Boulard et al. 2020).

496 Finally, the present chapter focused on measurements performed in “static” experiments. With the advent  
497 of gas-gun or laser-driven dynamic compression techniques coupled with either synchrotron or x-ray free  
498 electron lasers and faster detectors, time-resolved measurements at rapid strain rates are now achievable  
499 (e.g. Wehrenberg et al, 2017, Chen et al, 2019). Combined with deformation experiments at low strain  
500 rates, as described in this chapter, intermediate strain rate experiments in a dynamic diamond anvil cell  
501 (Méndez et al, 2020), and dynamic compression experiments will allow investigating the effect of orders  
502 of magnitude in strain rate on deformation and plasticity.

503

## 504 **6 Conclusion**

505 This chapter summarized the last 25 years of development of high pressure measurements of mechanical  
506 properties. The team around H.-K. Mao at the Carnegie Institution pioneered the development of radial x-  
507 ray diffraction in the DAC. The following years saw the development of LVP experiments, external-  
508 heating radial x-ray diffraction in the DAC, or multigrain crystallography. Conceptual advances, from the  
509 first theories of lattice strains in the 1990's to more advanced self-consistent calculations have also been a  
510 key component of such research. Early results and interpretation of high pressure deformation  
511 experiments lacked understanding of the fundamentals of plasticity and its effect on materials properties

512 and x-ray diffraction measurements. The introduction of self-consistent calculations was hence an  
513 important contribution to the field.

514 Nowadays, the studies of mechanical properties under extreme conditions is a thriving field of research,  
515 with applications in geosciences, for which it was first intended, but also materials sciences, as  
516 highlighted in the latest section of this chapter. Recent works, relying on multi-grain crystallography now  
517 allow the study of microstructures and plasticity at the grain scale and will open new doors to this field of  
518 research, offering a quantitative and comprehensive description of materials microstructure at the  
519 micrometre lengthscale. Strain mapping within a grain, along with the identification of deformation  
520 defects and densities is also within reach.

521 Plasticity depends on pressure, temperature, microstructures, but also strain rates. Further works should  
522 hence not only focus on extending the pressure and temperature conditions of the experiments, in order to  
523 reach those of the innermost sections of our planet, but also on exploring strain rates, from extremely fast  
524 processes at  $10^{10} \text{ s}^{-1}$  in a shock wave, to deep Earth conditions of  $10^{-15} \text{ s}^{-1}$ . To this day, this remains an  
525 experimental and numerical challenge.

## 526 **Acknowledgments**

527 The author would like to thank the two anonymous reviewers and N. Hilairet for constructive comments,  
528 as well as F. Lin for providing the raw data for Fig. 7. S. M. received support from the I-SITE UNLE  
529 grant MetalCore (R-ERCGEN-19-006-MERKEL).

## 530 **References**

- 531 Amodeo, J., Carrez, P. & Cordier, P. (2012). Modelling the effect of pressure on the critical shear stress of  
532 MgO single crystals. *Phil. Mag.*, 92, 1523–1541.
- 533 Amodeo, J., Dancette, S. & Delannay, L. (2016). Atomistically-informed crystal plasticity in MgO  
534 polycrystals under pressure. *Int. J. Plast.*, 82, 177–191.
- 535 Amodeo, J., Merkel, S., Tromas, C., Carrez, P., Korte-Kerzel, S., Cordier, P. & Chevalier, J. (2018).  
536 Dislocations and plastic deformation in MgO crystals: A review. *Crystals*, 8, 240.
- 537 Azuma, S., Nomura, R., Uesugi, K., Nakashima, Y., Kojima, Y., Doi, S. & Kakizawa, S. (2017). Anvil  
538 design for slip-free high pressure deformation experiments in a rotational diamond anvil cell. *High*  
539 *Pressure Research*, 38(1), 23–31.
- 540 Badro, J., Fiquet, G., Guyot, F., Rueff, J.-P., Struzhkin, V. V., Vankó, G. & Monaco, G. (2003). Iron  
541 partitioning in earth's mantle: Toward a deep lower mantle discontinuity. *Science*, 300, 789–791.
- 542 Blank, V., Konyaev, Y. S., Kuznetsov, A. I. & Estrin, E. (1984). Diamond chamber for examining the  
543 effects of shear deformation on the structure and properties of solids at pressures up to 43 GPa.  
544 *Instrum. Exp. Tech.*, 27, 1240–1242.
- 545 Boioli, F., Carrez, P., Cordier, P., Devincere, B., Gouriet, K., Hirel, P., Kraych, A. & Ritterbex, S. (2017).  
546 Pure climb creep mechanism drives flow in Earth's lower mantle. *Sci. Adv.*, 3(3), e1601958.
- 547 Boulard, E., Denoual, C., Dewaele, A., King, A., Godec, Y. L. & Guignot, N. (2020) Following the phase  
548 transitions of iron in 3D with X-ray tomography and diffraction under extreme conditions. *Acta*  
549 *Mater.*, 192, 30-39
- 550 Burnley, P. (2013). The importance of stress percolation patterns in rocks and other polycrystalline  
551 materials. *Nature Communications*, 4(1), 2117.
- 552 Chen, S., Li, Y., Zhang, N., Huang, J., Hou, H., Ye, S., Zhong, T., Zeng, X., Fan, D., Lu, L., Wang, L.,  
553 Sun, T., Fezzaa, K., Zhang, Y., Tang, M. & Luo, S. (2019). Capture Deformation Twinning in Mg  
554 during Shock Compression with Ultrafast Synchrotron X-Ray Diffraction. *Phys. Rev. Lett.*, 123,  
555 255501
- 556 Chen, B., Lutker, K., Raju, S. V., Yan, J., Kanitpanyacharoen, W., Lei, J., Yang, S., Wenk, H.-R., Mao, H.-  
557 K. & Williams, Q. (2012). Texture of nanocrystalline nickel: Probing the lower size limit of  
558 dislocation activity. *Science*, 338(6113), 1448–1451.
- 559 Chen, H., He, D., Liu, J., Li, Y., Peng, F., Li, Z., Wang, J. & Bai, L. (2010a). High-pressure radial x-ray  
560 diffraction study of osmium to 58 GPa. *Eur. Phys. J. B*, 73, 321–326.
- 561 Chen, H., Peng, F., Mao, H.-K., Shen, G., Liermann, H.-P., Li, Z. & Shu, J. (2010b). Strength and elastic  
562 moduli of TiN from radial x-ray diffraction under nonhydrostatic compression up to 45 GPa. *J.*  
563 *Appl. Phys.*, 107(11), 113503.
- 564 Clausen, B., Tomé, C. N., Brown, D. W. & Agnew, S. R. (2008). Reorientation and stress relaxation due  
565 to twinning: Modeling and experimental characterization for Mg. *Acta Mater.*, 56, 2456–2468.

566 Conil, N. & Kavner, A. (2006). Elastic behavior and strength of Al<sub>2</sub>O<sub>3</sub> fiber/Al matrix composite and  
567 implications for equation of state measurements in the diamond anvil cell. *J. Appl. Phys.*, 100,  
568 043517.

569 Cordier, P., Amodeo, J. & Carrez, P. (2012). Modelling the rheology of MgO under Earth's mantle  
570 pressure, temperature and strain rates. *Nature*, 481, 177-180.

571 Cordier, P. & Goryaeva, A. (Eds.) (2018). *Multiscale Modeling of the Mantle Rheology*. Lille, France.  
572 <https://lilloa.univ-lille.fr/handle/20.500.12210/5756>

573 Dewaele, A., Loubeyre, P., Occelli, F., Marie, O. & Mezouar, M. (2018). Toroidal diamond anvil cell for  
574 detailed measurements under extreme static pressures. *Nat. Commun.*, 9(1).

575 Dobson, D. P., Miyajima, N., Nestola, F., Alvaro, M., Casati, N., Liebske, C., Wood, I. G. & Walker,  
576 A. M. (2013). Strong inheritance of texture between perovskite and post-perovskite in the D''  
577 layer. *Nat. Geosci.*, 6, 575-578.

578 Dong, H., He, D., Duffy, T. S. & Zhao, Y. (2009). Elastic moduli and strength of nanocrystalline cubic  
579 BC<sub>2</sub>N from x-ray diffraction under nonhydrostatic compression. *Phys. Rev. B*, 79, 014105.

580 Duffy, T. S., Shen, G., Heinz, D. L., Shu, J., Ma, Y., Mao, H. K., Hemley, R. J. & Singh, A. K. (1999a).  
581 Lattice strains in gold and rhenium under non-hydrostatic compression to 37 GPa. *Phys. Rev. B*,  
582 60, 15063–15073.

583 Duffy, T. S., Shen, G., Shu, J., Mao, H. K., Hemley, R. J. & Singh, A. K. (1999b). Elasticity, shear  
584 strength and equation of state of molybdenum and gold from x-ray diffraction under  
585 nonhydrostatic compression to 24 GPa. *J. Appl. Phys.*, 86, 6729–6736.

586 Farla, R., Amulele, G., Girard, J., Miyajima, N. & Karato, S.-I. (2015). High-pressure and high-  
587 temperature deformation experiments on polycrystalline wadsleyite using the rotational drickamer  
588 apparatus. *Phys. Chem. Min.*, 42, 541–558.

589 Ferrand, T. P., Hilairet, N., Incel, S., Deldicque, D., Labrousse, L., Gasc, J., Renner, J., Wang, Y., II, H.  
590 W. G. & Schubnel, A. (2017). Dehydration-driven stress transfer triggers intermediate-depth  
591 earthquakes. *Nat. Commun.*, 8, 15247.

592 Girard, J., Amulele, G., Farla, R., Mohiuddin, A. & Karato, S.-I. (2016). Shear deformation of  
593 bridgmanite and magnesiowüstite aggregates at lower mantle conditions. *Science*, 351, 144–147.

594 Girard, J., Chen, J. & Raterron, P. (2012). Deformation of periclase single crystals at high pressure and  
595 temperature: Quantification of the effect of pressure on slip-system activities. *J. Appl. Phys.*, 111,  
596 112607.

597 Girard, J., Silber, R. E., Mohiuddin, A., Chen, H. & Karato, S. (2020) Development of a Stress Sensor for  
598 In-Situ High-Pressure Deformation Experiments Using Radial X-Ray Diffraction. *Minerals*, 10,  
599 166

600 Gleason, A. E. & Mao, W. L. (2013). Strength of iron at core pressures and evidence for a weak Earth's  
601 inner core. *Nat. Geosci.*, 6, 571-574.

602 He, D. & Duffy, T. S. (2006). X-ray diffraction study of the static strength of tungsten to 69 GPa. *Phys.*  
603 *Rev. B*, 73(13).

604 He, D., Shieh, S. & Duffy, T. (2004). Strength and equation of state of boron suboxide from radial x-ray  
605 diffraction in a diamond cell under nonhydrostatic compression. *Phys. Rev. B*, 70, 184121.

606 Heidelbach, F., Stretton, I., Langenhorst, F. & Mackwell, S. (2003). Fabric evolution during high shear  
607 strain deformation of magnesiowüstite ( $\text{Mg}_{0.8}\text{Fe}_{0.2}\text{O}$ ). *J. Geophys. Res.*, 108, 2154.

608 Hemley, R. J., Mao, H. K., Shen, G., Badro, J., Gillet, P., Hanfland, M. & Häusermann, D. (1997). X-ray  
609 imaging of stress and strain of diamond, iron & tungsten at megabar pressures. *Science*, 276,  
610 1242–1245.

611 Hruszkewycz, S. O., Allain, M., Holt, M. V., Murray, C. E., Holt, J. R., Fuoss, P. H. & Chamard, V.  
612 (2016). High-resolution three-dimensional structural microscopy by single-angle bragg  
613 ptychography. *Nature Materials*, 16(2), 244–251.

614 Hunt, S. A. & Dobson, D. P. (2017). Note: Modified anvil design for improved reliability in DT-cup  
615 experiments. *Rev. Sci. Instrum.*, 88, 126106.

616 Hunt, S. A., Weidner, D. J., McCormack, R. J., Whitaker, M. L., Bailey, E., Li, L., Vaughan, M. T. &  
617 Dobson, D. P. (2014). Deformation T-Cup: A new multi-anvil apparatus for controlled strain-rate  
618 deformation experiments at pressures above 18 GPa. *Rev. Sci. Instrum.*, 85, 085103.

619 Ice, G. E., Dera, P., Liu, W. & Mao, H.-K. (2005). Adapting polychromatic x-ray microdiffraction  
620 techniques to high-pressure research: energy scan approach. *J. Synchrotron Rad.*, 12, 608–617.

621 Immoor, J., Marquardt, H., Miyagi, L., Lin, F., Speziale, S., Merkel, S., Buchen, J., Kurnosov, A. &  
622 Liermann, H.-P. (2018). Evidence for  $\{100\}\langle 011\rangle$  slip in ferropericlase in earth's lower mantle  
623 from high-pressure/high-temperature experiments. *Earth Planet. Sci. Lett.*, 489, 251–257.

624 Immoor, J., Marquardt, H., Miyagi, L., Speziale, S., Merkel, S., Schwark, I., Ehnes, A. & Liermann, H.-P.  
625 (2020). An improved setup for radial diffraction experiments at high pressures and high  
626 temperatures in a resistive graphite-heated diamond anvil cell. *Rev. Sci. Instrum.*, 91(4), 045121.

627 Jeanloz, R. & Wenk, H.-R. (1988). Convection and anisotropy of the inner core. *Geophys. Res. Lett.*, 15,  
628 72–75.

629 Kaercher, P., Miyagi, L., Kanitpanyacharoen, W., Zepeda-Alarcon, E., Wang, Y., Parkinson, D.,  
630 Lebensohn, R., Carlo, F. D. & Wenk, H. (2016). Two-phase deformation of lower mantle mineral  
631 analogs. *Earth Planet. Sci. Lett.*, 456, 134–145.

632 Karato, S.-I., Forte, A., Liebermann, R., Masters, G. & Stixrude, L. (Eds.) (2000). *Earth's Deep Interior:  
633 Mineral Physics and Tomography From the Atomic to the Global Scale. Geophysical Monograph  
634 Series. Washington, DC: American Geophysical Union.*

635 Kasemer, M., Zepeda-Alarcon, E., Carson, R., Dawson, P. & Wenk, H.-R. (2020). Deformation  
636 heterogeneity and intragrain lattice misorientation in high strength contrast, dual-phase  
637 bridgmanite/periclase. *Acta Mater.*, 189, 284–298.

638 Kavner, A. & Duffy, T. S. (2003). Elasticity and rheology of platinum under high pressure and  
639 nonhydrostatic stress. *Phys. Rev. B*, 68, 144101.

640 Kawazoe, T., Karato, S. & O, J., Jing, Z., Otsuka, K. & Hustoft, J. W. (2010). Shear deformation of  
641 polycrystalline wadsleyite up to 2100 K at 14–17 GPa using a rotational drickamer apparatus  
642 (RDA). *J. Geophys. Res.*, 115, B08208.

643 Kawazoe, T., Ohuchi, T., Nishihara, Y., Nishiyama, N., Fujino, K. & Irifune, T. (2013). Seismic  
644 anisotropy in the mantle transition zone induced by shear deformation of wadsleyite. *Phys. Earth  
645 Planet. Int.*, 216, 91–98.

646 Kerber, M. B., Zehetbauer, M. J., Schafler, E., Spieckermann, F. C., Bernstorff, S. & Ungar, T. (2011). X-  
647 ray line profile analysis – An ideal tool to quantify structural parameters of nanomaterials. *JOM*,  
648 63, 61–70.

649 Kiefer, B., Shieh, S. R., Duffy, T. S. & Sekine, T. (2005). Strength, elasticity, and equation of state of the  
650 nanocrystalline cubic silicon nitride  $\gamma$ -Si<sub>3</sub>N<sub>4</sub> to 68 GPa. *Phys. Rev. B*, 72, 014102.

651 Kinsland, G. L. & Bassett, W. A. (1977). Strength of MgO and NaCl polycrystals to confining pressures  
652 of 250 kbar at 25 C. *J. Appl. Phys.*, 48, 978–984.

653 Kocks, U. F., Tomé, C. N. & Wenk, H.-R. (1998). *Texture and Anisotropy: Preferred Orientations and  
654 their Effects on Material Properties*. Cambridge: Cambridge Univ. Press.

655 Korte, S. & Clegg, W. (2011). Discussion of the dependence of the effect of size on the yield stress in  
656 hard materials studied by microcompression of MgO. *Philos. Mag.*, 91(7-9), 1150–1162.

657 Kumar, M. A., Hilairet, N., McCabe, R., Yu, T., Wang, Y., Beyerlein, I. & Tomé, C. (2020). Role of  
658 twinning on the omega-phase transformation and stability in zirconium. *Acta Mater.*, 185, 211–  
659 217.

660 Langrand, C., Hilairet, N., Nisr, C., Roskosz, M., Ribárik, G., Vaughan, G. B. M. & Merkel, S. (2017).  
661 Reliability of multigrain indexing for orthorhombic polycrystals above 1mbar: application to  
662 MgSiO<sub>3</sub> post-perovskite. *J. Appl. Crystallogr.*, 50, 120–130.

663 Lebensohn, R. A. & Tomé, C. N. (1994). A self-consistent visco-plastic model: calculation of rolling  
664 textures of anisotropic materials. *Mater. Sci. Eng. A*, 175, 71–82.

665 Levitas, V. I. (2004). High-pressure mechanochemistry: Conceptual multiscale theory and interpretation  
666 of experiments. *Phys. Rev. B*, 70, 184118.

667 Li, L., Weidner, D. J., Chen, J., Vaughan, M. T., Davis, M. & Durham, W. B. (2004). X-ray strain analysis  
668 at high pressure: Effect of plastic deformation in MgO. *J. Appl. Phys.*, 95, 8357–8365.

669 Liermann, H.-P., Merkel, S., Miyagi, L., Wenk, H.-R., Shen, G., Cynn, H. & Evans, W. J. (2009). New  
670 experimental method for in situ determination of material textures at simultaneous high-pressure  
671 and temperature by means of radial diffraction in the diamond anvil cell. *Rev. Sci. Instrum.*, 80,  
672 104501.

673 Liermann, H. P., Singh, A. K., Somayazulu, M. & Saxena, S. K. (2007). Compression behavior of NbC  
674 under nonhydrostatic conditions to 57 GPa. *Int. J. Refract. Met. Hard Mater.*, 25, 386–391.

675 Lin, F., Couper, S., Jogle, M. & Miyagi, L. (2019). Competing deformation mechanisms in periclase:  
676 Implications for lower mantle anisotropy. *Minerals*, 9, 650.

677 Lin, F., Hilairet, N., Raterron, P., Addad, A., Immoor, J., Marquardt, H., Tomé, C., Miyagi, L. & Merkel,  
678 S. (2017). Elasto-viscoplastic self consistent modeling of the ambient temperature plastic behavior  
679 of periclase deformed up to 5.4 GPa. *J. Appl. Phys.*, 122, 205902.

680 Lin, J. F., Wenk, H.-R., Voltolini, M., Speziale, S., Shu, J. & Duffy, T. S. (2009). Deformation of lower-  
681 mantle ferroperricite (Mg,Fe)O across the electronic spin transition. *Phys. Chem. Min.*, 36, 585–  
682 592.

683 Lincot, A., Cardin, P., Deguen, R. & Merkel, S. (2016). Multiscale model of global inner-core anisotropy  
684 induced by hcp alloy plasticity. *Geophys. Res. Lett.*, 43, 1084–1091.

685 Long, M. D., Xiao, X., Jiang, Z., Evans, B. & Karato, S. (2006). Lattice preferred orientation in  
686 deformed polycrystalline (Mg,Fe)O and implications for seismic anisotropy in D". *Phys. Earth  
687 Planet. Inter.*, 156, 75–88.

688 Ludwig, W., King, A., Reischig, P., Herbig, M., Lauridsen, E., Schmidt, S., Proudhon, H., Forest, S.,  
689 Cloetens, P., du Roscoat, S. R., Buffière, J., Marrow, T. & Poulsen, H. (2009). New opportunities  
690 for 3D materials science of polycrystalline materials at the micrometre lengthscale by combined  
691 use of x-ray diffraction and x-ray imaging. *Mat. Sci. Eng. A*, 524, 69–76.

692 Lutterotti, L., Matthies, S. & Wenk, H.-R. (1999). MAUD: a friendly Java program for materials analysis  
693 using diffraction. *IUCr: Newsletter of the CPD*, 21, 14–15.

694 Ma, Y., Selvi, E., Levitas, V. I. & Hashemi, J. (2006). Effect of shear strain on the  $\alpha$ - $\epsilon$  phase transition of  
695 iron: a new approach in the rotational diamond anvil cell. *J. Phys.: Condens. Matter*, 18, S1075–  
696 S1082.

697 Mainprice, D., Barruol, G. & Ismail, W. B. (2000). The seismic anisotropy of the earth's mantle: from  
698 single crystal to polycrystal. In S. Karato, A. M. Forte, R. C. Liebermann, G. Master & L. Stixrude  
699 (Eds.) *Earth's Deep Interior. Mineral Physics and Tomography. From the Atomic to the Global  
700 Scale*, (pp. 237–264). Washington, DC: Am. Geophys. Union.

701 Mandolini, T., Hilairt, N., Chantel, J., Merkel, S., Le Godec, Y., Guignot, N. & King, A. (2020)  
702 Microstructural evolution in deforming olivine-serpentine aggregates at subduction zones  
703 conditions using in-situ X-ray tomography, AGU Fall Meeting, MR028-06

704 Mao, H. K., Shu, J., Shen, G., Hemley, R. J., Li, B. & Singh, A. K. (1998). Elasticity and rheology of iron  
705 above 220 GPa and the nature of the earth's inner core. *Nature*, 396, 741–743. Correction, *Nature*  
706 399, 280, 1999.

707 Marquardt, H. & Miyagi, L. (2015). Slab stagnation in the shallow lower mantle linked to an increase in  
708 mantle viscosity. *Nat. Geosci.*, 8, 311–314.

709 Meade, C. & Jeanloz, R. (1988) Yield strength of MgO to 40 GPa. *J. Geophys. Res.*, 93, 3261–3269

710 Mei, S., Kohlstedt, D. L., Durham, W. B. & Wang, L. (2008). Experimental investigation of the creep  
711 behavior of MgO at high pressures. *Phys. Earth Planet. Inter.*, 170, 170–175.

712 Méndez, A. S. J., Marquardt, H., Husband, R. J., Schwark, I., Mainberger, J., Glazyrin, K., Kurnosov, A.,  
713 Otzen, C., Satta, N., Bednarcik, J. & Liermann, H.-P. (2020) A resistively-heated dynamic  
714 diamond anvil cell (RHdDAC) for fast compression x-ray diffraction experiments at high  
715 temperatures. *Rev. Sci. Instrum.*, 91, 073906

716 Merkel, S., Gruson, M., Wang, Y., Nishiyama, N. & Tomé, C. N. (2012). Texture and elastic strains in  
717 hcp-iron plastically deformed up to 17.5 GPa and 600 K: experiment and model. *Modelling Simul.  
718 Mater. Sci. Eng.*, 20, 024005.



719 Merkel, S. & Hilairret, N. (2015). Multifit/polydefix: a framework for the analysis of polycrystal  
720 deformation using x-rays. *J. Appl. Cryst.*, 48, 1307–1313.

721 Merkel, S., McNamara, A. K., Kubo, A., Speziale, S., Miyagi, L., Meng, Y., Duffy, T. S. & Wenk, H.-R.  
722 (2007). Deformation of (Mg,Fe)SiO<sub>3</sub> post-perovskite and D” anisotropy. *Science*, 316, 1729 –  
723 1732.

724 Merkel, S., Miyajima, N., Antonangeli, D., Fiquet, G. & Yagi, T. (2006). Lattice preferred orientation and  
725 stress in polycrystalline hcp-Co plastically deformed under high pressure. *J. Appl. Phys.*, 100,  
726 023510.

727 Merkel, S., Tomé, C. N. & Wenk, H.-R. (2009). A modeling analysis of the influence of plasticity on high  
728 pressure deformation of hcp-Co. *Phys. Rev. B*, 79, 064110.

729 Merkel, S., Wenk, H.-R., Gillet, P., Mao, H. K. & Hemley, R. J. (2004). Deformation of polycrystalline  
730 iron up to 30 GPa and 1000 K. *Phys. Earth Planet. Inter.*, 145, 239–251.

731 Merkel, S., Wenk, H.-R., Shu, J., Shen, G., Gillet, P., Mao, H. K. & Hemley, R. J. (2002). Deformation of  
732 polycrystalline MgO at pressures of the lower mantle. *J. Geophys. Res.*, 107, 2271.

733 Merkel, S. & Yagi, T. (2005). X-ray transparent gasket for diamond anvil cell high pressure experiments.  
734 *Rev. Sci. Instrum.*, 76, 046109.

735 Miyagi, L., Amulele, G., Otsuka, K., Du, Z., Farla, R. & Karato, S. (2014). Plastic anisotropy and slip  
736 systems in ringwoodite deformed to high shear strain in the rotational Drickamer apparatus. *Phys.*  
737 *Earth Planet. Int.*, 228, 244–253.

738 Miyagi, L., Kanitpanyacharoen, W., Kaercher, P., Lee, K. K. M. & Wenk, H.-R. (2010). Slip systems in  
739 MgSiO<sub>3</sub> post-perovskite: Implications for D” anisotropy. *Science*, 329, 1639 – 1641.

740 Miyagi, L., Kunz, M., Knight, J., Nasiatka, J., Voltolini, M. & Wenk, H.-R. (2008). In situ phase  
741 transformation and deformation of iron at high pressure and temperature. *J. Appl. Phys.*, 104,  
742 103510.

743 Miyagi, L., Kanitpanyacharoen, W., Raju, S. V., Kaercher, P., Knight, J., MacDowell, A., Wenk, H.-R.,  
744 Williams, Q. & Alarcon, E. Z. (2013). Combined resistive and laser heating technique for in situ  
745 radial X-ray diffraction in the diamond anvil cell at high pressure and temperature. *Rev. Sci.*  
746 *Instrum.*, 84, 025118

747 Miyagi, L. & Wenk, H.-R. (2016). Texture development and slip systems in bridgmanite and bridgmanite  
748 + ferropericlasite aggregates. *Phys Chem Minerals*, 43(8), 597–613.

749 Mohiuddin, A., Karato, S. & Girard, J. (2020) Slab weakening during the olivine to ringwoodite transition  
750 in the mantle. *Nat. Geosci.*, 13, 170-174

751 Muránsky, O., Barnett, M., Carr, D., Vogel, S. & Oliver, E. (2010). Investigation of deformation twinning  
752 in a fine-grained and coarse-grained ZM20 mg alloy: Combined in situ neutron diffraction and  
753 acoustic emission. *Acta Mater*, 58(5), 1503–1517.

754 Naik, S. N. & Walley, S. M. (2020). The hall–petch and inverse hall–petch relations and the hardness of  
755 nanocrystalline metals. *J. Mater. Sci.*, 55(7), 2661–2681.

756 Neil, C. J., Wollmershauser, J. A., Clausen, B., Tomé, C. N. & Agnew, S. R. (2010) Modeling lattice strain  
757 evolution at finite strains and experimental verification for copper and stainless steel using in situ  
758 neutron diffraction. *Int. J. Plasticity*, 26, 1772–1791

759 Nishihara, Y., Ohuchi, T., Kawazoe, T., Seto, Y., Maruyama, G., Higo, Y., Funakoshi, K.-I., Tange, Y. &  
760 Irifune, T. (2018). Deformation-induced crystallographic-preferred orientation of hcp-iron: An  
761 experimental study using a deformation-DIA apparatus. *Earth Planet. Sci. Lett.*, 490, 151–160.

762 Nishihara, Y., Tinker, D., Kawazoe, T., Xu, Y., Jing, Z., Matsukage, K. N. & Karato, S. (2008). Plastic  
763 deformation of wadsleyite and olivine at high-pressure and high-temperature using a rotational  
764 Drickamer apparatus (RDA). *Phys. Earth Planet. Inter.*, 170, 156–169.

765 Nisr, C., Ribárik, G., Ungár, T., Vaughan, G. B. & Merkel, S. (2014). Three-dimensional x-ray diffraction  
766 in the diamond anvil cell: application to stishovite. *High Pres. Res.*, 34, 158–166.

767 Nisr, C., Ribárik, G., Ungár, T., Vaughan, G. B. M., Cordier, P. & Merkel, S. (2012). High resolution  
768 three-dimensional x-ray diffraction study of dislocations in grains of MgGeO<sub>3</sub> post-perovskite at  
769 90 GPa. *J. Geophys. Res.*, 117, B03201.

770 Nomura, R., Azuma, S., Uesugi, K., Nakashima, Y., Irifune, T., Shinmei, T., Kakizawa, S., Kojima, Y. &  
771 Kadobayashi, H. (2017). High-pressure rotational deformation apparatus to 135 GPa. *Rev. Sci.*  
772 *Instrum.*, 88, 044501.

773 Noyan, I. & Cohen, J. (1987). *Residual stress: measurements by diffraction and interpretation*. New-York:  
774 Springer-Verlag.

775 Nzogang, B. C., Bouquerel, J., Cordier, P., Mussi, A., Girard, J. & Karato, S. (2018). Characterization by  
776 scanning precession electron diffraction of an aggregate of bridgmanite and ferropericlasite  
777 deformed at HP-HT. *Geochem. Geophys. Geosyst.*, 19(3), 582–594.

778 Oddershede, J., Schmidt, S., Poulsen, H. F., Sorensen, H. O., Wright, J. & Reimers, W. (2010).  
779 Determining grain resolved stresses in polycrystalline materials using three-dimensional x-ray  
780 diffraction. *J. Appl. Cryst.*, 43, 539–549.

781 Paterson, M. S. & Weaver, C. W. (1970). Deformation of polycrystalline MgO under pressure. *J. Am.*  
782 *Ceram. Soc.*, 53, 463–471.

783 Philippe, J., Godec, Y. L., Mezouar, M., Berg, M., Bromiley, G., Bergame, F., Perrillat, J. P., Alvarez-  
784 Murga, M., Morand, M., Atwood, R., King, A. & Régnier, S. (2016) Rotating tomography Paris–  
785 Edinburgh cell: a novel portable press for micro-tomographic 4-D imaging at extreme  
786 pressure/temperature/stress conditions. *High Pressure Research*, 36, 512–532

787 Poulsen, H. F. (2004). *Three-Dimensional X-Ray Diffraction Microscopy: Mapping Polycrystals and their*  
788 *Dynamics*. vol. 205 of Springer Tracts in Modern Physics. Berlin, Heidelberg, Germany: Springer.

789 Raterron, P. & Merkel, S. (2009). In situ rheological measurements at extreme pressure and temperature  
790 using synchrotron x-ray diffraction and radiography. *J. Synchrotron Radiat.*, 16, 748–756.

791 Reali, R., Jackson, J., Orman, J. V., Bower, D., Carrez, P. & Cordier, P. (2019). Modeling viscosity of  
792 (Mg,Fe)O at lowermost mantle conditions. *Phys. Earth Planet. Inter.*, 287, 65–75.

793 Reynard, B., Caracas, R., Cardon, H., Montagnac, G. & Merkel, S. (2019). High-pressure yield strength  
794 of rocksalt structures using quartz raman piezometry. *C.R. Geosci.*, 351(2-3), 71–79.

795 Ribárik, G., Jóni, B. & Ungár, T. (2019) Global optimum of microstructure parameters in the CMWP line-  
796 profile-analysis method by combining Marquardt-Levenberg and Monte-Carlo procedures. *J.*  
797 *Mater. Sci. Technol.*, 35, 1508-1514

798 Rosa, A. D., Hilairret, N., Ghosh, S., Perrillat, J.-P., Garbarino, G. & Merkel, S. (2016). Evolution of grain  
799 sizes and orientations during phase transitions in hydrous Mg<sub>2</sub>SiO<sub>4</sub>. *J. Geophys. Res.*, 121, 7161–  
800 7176.

801 Schmidt, S. (2014). Grainspotter: a fast and robust polycrystalline indexing algorithm. *J Appl Cryst*, 47,  
802 276–284.

803 Schropp, A., Hoppe, R., Meier, V., Patommel, J., Seiboth, F., Ping, Y., Hicks, D. G., Beckwith, M. A.,  
804 Collins, G. W., Higginbotham, A., Wark, J. S., Lee, H. J., Nagler, B., Galtier, E. C., Arnold, B.,  
805 Zastrau, U., Hastings, J. B. & Schroer, C. G. (2015). Imaging Shock Waves in Diamond with Both  
806 High Temporal and Spatial Resolution at an XFEL. *Sci. Rep.*, 5, 11089

807 Schubnel, A., Brunet, F., Hilairret, N., Gasc, J., Wang, Y. & Green II, H. W. (2013). Deep-focus earthquake  
808 analogs recorded at high pressure and temperature in the laboratory. *Science*, 341, 1377–1380.

809 Sedmák, P., Pilch, J., Heller, L., Kopeček, J., Wright, J., Sedlák, P., Frost, M. & Šittner, P. (2016). Grain-  
810 resolved analysis of localized deformation in nickel-titanium wire under tensile load. 353, 559–  
811 562.

812 Simons, H., King, A., Ludwig, W., Detlefs, C., Pantleon, W., Schmidt, S., Stöhr, F., Snigireva, I., Snigirev,  
813 A. & Poulsen, H. F. (2015). Dark-field x-ray microscopy for multiscale structural characterization.  
814 *Nature Communications*, 6(1), 6098.

815 Singh, A. K., Balasingh, C., Mao, H. K., Hemley, R. J. & Shu, J. (1998). Analysis of lattice strains  
816 measured under non-hydrostatic pressure. *J. Appl. Phys.*, 83, 7567–7575.

817 Singh, A. K., Liermann, H., Akahama, Y., Saxena, S. K. & Menéndez-Proupin, E. (2008). Strength of  
818 polycrystalline coarse-grained platinum to 330 GPa and of nanocrystalline platinum to 70 GPa  
819 from high-pressure x-ray diffraction data. *J. Appl. Phys.*, 103, 063524.

820 Singh, A. K., Liermann, H.-P., Akahama, Y. & Kawamura, H. (2007). Aluminum as a pressure-  
821 transmitting medium cum pressure standard for x-ray diffraction experiments to 200 GPa with  
822 diamond anvil cells. *J. Appl. Phys.*, 101, 123526.

823 Stretton, I., Heidelberg, F., Mackwell, S. & Langenhorst, F. (2001). Dislocation creep of magnesiowüstite  
824 (Mg<sub>0.8</sub>Fe<sub>0.2</sub>O). *Earth Planet. Sci. Lett.*, 194, 229–240.

825 Tateno, S., Hirose, K., Ohishi, Y. & Tatsumi, Y. (2010). The structure of iron in Earth's inner core.  
826 *Science*, 330, 359 – 361.

827 Todd, K. A., Watson, H. C., Yu, T. & Wang, Y. (2016) The effects of shear deformation on planetesimal  
828 core segregation: Results from in-situ X-ray micro-tomography. *Am. Mineral.*, 101, 1996-2004

829 Tommaseo, C. E., Devine, J., Merkel, S., Speziale, S. & Wenk, H.-R. (2006). Texture development and  
830 elastic stresses in magnesiowüstite at high pressure. *Phys. Chem. Miner.*, 33, 84–97.

831 Tromas, C., Girard, J. C. & Woïrgard, J. (2000). Study by atomic force microscopy of elementary  
832 deformation mechanisms involved in low load indentations in MgO crystals. *Philos. Mag. A*, 80,  
833 2325–2335.

- 834 Tsujino, N., Nishihara, Y., Yamazaki, D., Seto, Y., Higo, Y. & Takahashi, E. (2016). Mantle dynamics  
835 inferred from the crystallographic preferred orientation of bridgmanite. *Nature*, 539, 81–84.
- 836 Turner, P. A. & Tomé, C. N. (1994). A study of residual stresses in zircaloy-2 with rod texture. *Acta*  
837 *Metall. Mater.*, 42, 4143–4153.
- 838 Uchida, T., Wang, Y., Rivers, M. L. & Sutton, S. R. (2004). Yield strength and strain hardening of MgO  
839 up to 8 GPa measured in the deformation-DIA with monochromatic x-ray diffraction. *Earth Planet.*  
840 *Sci. Lett.*, 226, 117–126.
- 841 Urakawa, S., Terasaki, H. P., Funakoshi, K., Uesugi, K. & Yamamoto, S. (2010) Development of high  
842 pressure apparatus for X-ray microtomography at Spring-8. *J. Phys.: Conf. Ser.*, 215, 012026
- 843 Vinogradov, A., Vasilev, E., Seleznev, M., Máthis, K., Orlov, D. & Merson, D. (2016). On the limits of  
844 acoustic emission detectability for twinning. *Mater. Lett.*, 183, 417–419.
- 845 Wallis, D., Hansen, L. N., Britton, T. B. & Wilkinson, A. J. (2017). Dislocation interactions in olivine  
846 revealed by HR-EBSD. *J. Geophys. Res. Solid Earth*, 122, 7659–7678.
- 847 Wang, H., Wu, P. D., Tomé, C. N. & Huang, Y. (2010). A finite strain elastic-viscoplastic self-consistent  
848 model for polycrystalline materials. *J. Mech. Phys. Solids*, 58, 594–612.
- 849 Wang, Y., Duhram, W. B., Getting, I. C. & Weidner, D. J. (2003). The deformation-DIA: A new apparatus  
850 for high temperature triaxial deformation to pressures up to 15 GPa. *Rev. Sci. Instrum.*, 74, 3002–  
851 3011.
- 852 Wang, Y., Leshner, C., Fiquet, G., Rivers, M. L., Nishiyama, N., Siebert, J., Roberts, J., Morard, G.,  
853 Gaudio, S., Clark, A., Watson, H., Menguy, N. & Guyot, F. (2011). In situ high-pressure and high-  
854 temperature X-ray microtomographic imaging during large deformation: A new technique for  
855 studying mechanical behavior of multiphase composites. *Geosphere*, 7, 40–53.
- 856 Wang, Y., Hilairet, N., Nishiyama, N., Yahata, N., Tsuchiya, T., Morard, G. & Fiquet, G. (2013). High-  
857 pressure, high-temperature deformation of CaGeO<sub>3</sub> (perovskite)±MgO aggregates: Implications  
858 for multiphase rheology of the lower mantle. *Geochem. Geophys. Geosyst.*, 14, 3389–3408.
- 859 Wang, Y. & Shen, G. (2014). High-pressure experimental studies on geo-liquids using synchrotron  
860 radiation at the Advanced Photon Source. *J. Earth Sci.*, 25, 939–958.
- 861 Wang, Y., Zhu, L., Shi, F., Schubnel, A., Hilairet, N., Yu, T., Rivers, M., Gasc, J., Addad, A., Deldicque,  
862 D., Li, Z. & Brunet, F. (2017). A laboratory nanoseismological study on deep-focus earthquake  
863 micromechanics. *Sci. Adv.*, 3(7), e1601896.
- 864 Wehrenberg, C. E., McGonegle, D., Bolme, C., Higginbotham, A., Lazicki, A., Lee, H. J., Nagler, B.,  
865 Park, H.-S., Remington, B. A., Rudd, R. E., Sliwa, M., Suggit, M., Swift, D., Tavella, F., Zepeda-  
866 Ruiz, L., Wark, J. S. (2017). In situ X-ray diffraction measurement of shock-wave-driven twinning  
867 and lattice dynamics. *Nature*, 550, 496–499
- 868 Weinberger, M. B., Tolbert, S. H. & Kavner, A. (2008). Osmium metal studied under high pressure and  
869 nonhydrostatic stress. *Phys. Rev. Lett.*, 100, 045506.
- 870 Weiss, J., Lahaie, F. & Grasso, J. R. (2000). Statistical analysis of dislocation dynamics during  
871 viscoplastic deformation from acoustic emission. *J. Geophys. Res.*, 105, 433–442.

872 Wenk, H.-R., Kaercher, P., Kanitpanyacharoen, W., Zepeda-Alarcon, E. & Wang<sup>2</sup>, Y. (2013). Orientation  
873 relations during the  $\alpha$ - $\omega$  phase transition of zirconium: In situ texture observations at high pressure  
874 and temperature. *Phys. Rev. Lett.*, 111, 195701.

875 Wenk, H.-R., Lonardelli, I., Merkel, S., Miyagi, L., Pehl, J., Speziale, S. & Tommaseo, C. E. (2006).  
876 Deformation textures produced in diamond anvil experiments, analysed in radial diffraction  
877 geometry. *J. Phys.: Condens. Matter*, 18, S933–S947.

878 Wenk, H.-R., Lutterotti, L., Kaercher, P., Kanitpanyacharoen, W., Miyagi, L. & Vasin, R. (2014). Rietveld  
879 texture analysis from synchrotron diffraction images. ii. complex multiphase materials and  
880 diamond anvil cell experiments. *Powder Diffr.*, 29, 220–232.

881 Wenk, H.-R., Matthies, S., Donovan, J. & Chateigner, D. (1998). Beartex: a windows-based program  
882 system for quantitative texture analysis. *J. Appl. Cryst.*, 31, 262–269.

883 Wenk, H.-R., Matthies, S., Hemley, R. J., Mao, H. K. & Shu, J. (2000). The plastic deformation of iron at  
884 pressures of the Earth's inner core. *Nature*, 405, 1044–1047.

885 Xiong, L., Li, B., Tang, Y., Li, Q., Hao, J., Bai, L., Li, X. & Liu, J. (2018). Radial x-ray diffraction study  
886 of the static strength and texture of tungsten to 96 GPa. *Solid State Commun.*, 269, 83–89.

887 Xiong, L., Liu, J., Bai, L., Li, X., Lin, C. & Lin, J.-F. (2014). Strength and structural phase transitions of  
888 gadolinium at high pressure from radial x-ray diffraction. *J. Appl. Phys.*, 116, 243503.

889 Xiong, L., Liu, J., Bai, L., Li, Y., Lin, C., He, D., Peng, F. & Lin, J.-F. (2013). Radial x-ray diffraction of  
890 tungsten tetraboride to 86 GPa under nonhydrostatic compression. *J. Appl. Phys.*, 113, 033507.

891 Xu, Y., Nishihara, Y. & Karato, S. (2005). Development of a rotational drickamer apparatus for large-  
892 strain deformation experiments at deep earth conditions. In J. Chen, Y. Wang, T. S. Duffy, G. Shen  
893 & L. F. Dobrzhinetskaya (Eds.) *Advances in High-Pressure Technology for Geophysical*  
894 *Applications*, (pp. 167–182). Amsterdam: Elsevier.

895 Yamazaki, D. & Karato, S. (2001). High-pressure rotational deformation apparatus to 15 GPa. *Rev. Sci.*  
896 *Instrum.*, 72, 4207–4211.

897 Yamazaki, D. & Karato, S. (2002). Fabric development in (Mg,Fe)O during large strain, shear  
898 deformation: implications for seismic anisotropy in Earth's lower mantle. *Phys. Earth Planet.*  
899 *Inter.*, 131, 251–267.

900 Yang, W., Huang, X., Harder, R., Clark, J. N., Robinson, I. K. & Mao, H.K. (2013). Coherent diffraction  
901 imaging of nanoscale strain evolution in a single crystal under high pressure. *Nature*  
902 *Communications*, 4(1), 1680.

903 Yau, A., Cha, W., Kanan, M. W., Stephenson, G. B. & Ulvestad, A. (2017). Bragg coherent diffractive  
904 imaging of single-grain defect dynamics in polycrystalline films. *Science*, 356(6339), 739–742.

905 Yu, X., Zhang, R., Weldon, D., Vogel, S. C., Zhang, J., Brown, D. W., Wang, Y., Reiche, H. M., Wang, S.,  
906 Du, S., Jin, C. & Zhao, Y. (2015). High pressure phase-transformation induced texture evolution  
907 and strengthening in zirconium metal: Experiment and modeling. *Sci. Rep.*, 5, 12552.

908 Yu, T., Wang, Y. & Rivers, M. L. (2016) Imaging in 3D under pressure: a decade of high-pressure X-ray  
909 microtomography development at GSECARS. *Prog. Earth Planet. Sci.*, 3, 17

910 Yue, B., Hong, F., Merkel, S., Tan, D., Yan, J., Chen, B. & Mao, H.-K. (2016). Deformation behavior  
911 across the zircon-scheelite phase transition. 117, 135701.

912 Zarechnyy, O. M., Levitas, V. I. & Ma, Y. (2012). Coupled plastic flow and phase transformation under  
913 compression of materials in a diamond anvil cell: Effects of transformation kinetics and yield  
914 strength. *J. Appl. Phys.*, 111, 023518.

915 Zhang, L., Meng, Y., Yang, W., Wang, L., Mao, W. L., Zeng, Q.-S., Jeong, J. S., Wagner, A. J., Mkhoyan,  
916 K. A., Liu, W., Xu, R. & Mao, H.K (2014). Disproportionation of (Mg,Fe)SiO<sub>3</sub> perovskite in  
917 Earth's deep lower mantle. *Science*, 344, 877–882.

918 Zhou, X., Feng, Z., Zhu, L., Xu, J., Miyagi, L., Dong, H., Sheng, H., Wang, Y., Li, Q., Ma, Y., Zhang, H.,  
919 Yan, J., Tamura, N., Kunz, M., Lutker, K., Huang, T., Hughes, D. A., Huang, X. & Chen, B.  
920 (2020). High-pressure strengthening in ultrafine-grained metals. *Nature*, 579 (7797), 67-72.

921